

## Classical density functional theory of orientational order at interfaces: Application to water

Khuloud Jaqaman, Kagan Tuncay, and Peter J. Ortoleva

Citation: *The Journal of Chemical Physics* **120**, 926 (2004); doi: 10.1063/1.1630012

View online: <http://dx.doi.org/10.1063/1.1630012>

View Table of Contents: <http://scitation.aip.org/content/aip/journal/jcp/120/2?ver=pdfcov>

Published by the [AIP Publishing](#)

---

### Advertisement:



## Re-register for Table of Content Alerts

Create a profile.



Sign up today!



# Classical density functional theory of orientational order at interfaces: Application to water

Khuloud Jaqaman

*Department of Chemistry, Indiana University, Bloomington, Indiana 47405 and Center for Integrative Molecular Biosciences, The Scripps Research Institute, San Diego, California 92121*

Kagan Tuncay and Peter J. Ortoleva

*Department of Chemistry, Indiana University, Bloomington, Indiana 47405*

(Received 9 June 2003; accepted 6 October 2003)

A classical density functional formalism has been developed to predict the position-orientation number density of structured fluids. It is applied to the liquid–vapor interface of pure water, where it consists of a classical term, a gradient correction, and an anisotropic term that yields order through density gradients. The model is calibrated to predict that water molecules have their dipole moments almost parallel to a planar interface, while the molecular plane is parallel to it on the liquid side and perpendicular to it on the vapor side. For a planar interface, the surface tension obtained is twice its experimental value, while the surface potential is in qualitative agreement with that calculated by others. The model is also used to predict the orientation of water molecules near the surface of droplets, as well as the dependence of equilibrium vapor pressure around them on their size.

© 2004 American Institute of Physics. [DOI: 10.1063/1.1630012]

## I. INTRODUCTION

Although bulk water in the liquid or vapor phase is isotropic at room temperature and pressure, net orientational order at the interface has been observed experimentally,<sup>1–3</sup> in molecular dynamics simulations<sup>4–9</sup> and through phenomenological density functional calculations.<sup>10–14</sup> The nature of this orientation is an important issue in the study of mesoscopic phenomena, such as the interface between two homogeneous phases or the disturbance of a homogeneous phase due to the immersion of a macromolecule in it.

Although quantum mechanics and mixed quantum/classical molecular dynamics simulations yield the most detailed information about an interface, they are time consuming and suffer from statistical sampling errors.<sup>15</sup> Treating water as a continuum is an attractive alternative, in which case a density functional approach must be used to model the profile and orientational structure at the interface. However, recent density functional studies of the liquid–vapor interface<sup>12–14</sup> are not in good agreement with molecular dynamics simulations as regards the orientation of the molecular plane and the dipole moment on the vapor side.

In this paper, we use a field theoretical approach to devise a phenomenological expression for the Helmholtz free energy of fluids that accounts for molecular structure. The expression contains a sufficient number of terms to model the phenomenon of interest. We apply this approach to determine the position-orientation density of water molecules at the liquid–vapor interface. The parameters of the model are determined by fitting results to those of the molecular dynamics simulations by Sokhan and Tildesley<sup>7</sup> since the SPC/E water model<sup>16</sup> used in these simulations is one of the better potentials available.<sup>17,18</sup> Furthermore, they use a relatively large number of water molecules in their simulations

and account for long range electrostatic interactions accurately through the Ewald summation technique.<sup>19</sup>

## II. FORMULATION

### A. Descriptive variables

To identify a set of variables that describe the medium, first consider a molecule of arbitrary composition and shape, treated as a rigid body. It has three translational and three rotational degrees of freedom. The three translational degrees of freedom can be taken as the position,  $\mathbf{r}$ , of an arbitrary point in the molecule (point C in Fig. 1), such as its center of mass or its center of absolute charge. The three rotational degrees of freedom are best described by the three Euler angles,  $\Omega \equiv (\phi, \theta, \chi)$ , which represent the rotation of a set of body-fixed axes centered at C ( $x_b y_b z_b$ -frame in Fig. 1) about a coordinate system that is also centered at C ( $x' y' z'$ -frame in Fig. 1) but is always parallel to the space-fixed coordinate system ( $x y z$ -frame in Fig. 1). The three Euler angles used in our model follow the  $y$ -convention.<sup>20</sup>

Based on this description of one molecule, a collection of  $N$  molecules treated as a continuum is characterized by its position-orientation number density  $\rho(\mathbf{r}, \Omega)$ . By normalization,

$$\int d\mathbf{r} d\Omega \rho(\mathbf{r}, \Omega) = N. \quad (1)$$

In practice, both for computational and model development reasons, it is convenient to divide  $\rho$  into two parts: one orientation-dependent and another orientation-independent. The motivation for this division is seen by expanding  $\rho$  in generalized spherical harmonics:

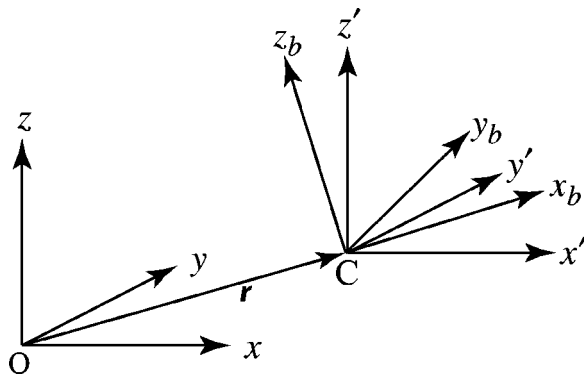


FIG. 1. Relation between space-fixed ( $xyz$ ) and body-fixed ( $x_b, y_b, z_b$ ) coordinates. The intermediate set ( $x', y', z'$ ) moves with the body but is always parallel to the space fixed set.

$$\rho(\mathbf{r}, \Omega) \equiv \sum_{l=0}^{\infty} \sum_{m=-l}^l \sum_{n=-l}^l \rho_{lmn}(\mathbf{r}) D_{mn}^l(\Omega)^*, \quad (2)$$

where

$$\rho_{lmn}(\mathbf{r}) = \frac{2l+1}{8\pi^2} \int d\Omega D_{mn}^l(\Omega) \rho(\mathbf{r}, \Omega). \quad (3)$$

Since the  $\rho_{lmn}$  are independent,  $\rho$  can be divided into two independent parts,

$$\rho(\mathbf{r}, \Omega) \equiv \rho^0(\mathbf{r}) + \rho^1(\mathbf{r}, \Omega), \quad (4)$$

without any loss of generality. The two terms are given by

$$\rho^0(\mathbf{r}) \equiv \rho_{000}(\mathbf{r}) = \frac{1}{8\pi^2} \int d\Omega \rho(\mathbf{r}, \Omega) \quad (5)$$

and

$$\begin{aligned} \rho^1(\mathbf{r}, \Omega) &\equiv \sum_{l=1}^{\infty} \sum_{m=-l}^l \sum_{n=-l}^l \rho_{lmn}(\mathbf{r}) D_{mn}^l(\Omega)^* \\ &= \rho(\mathbf{r}, \Omega) - \frac{1}{8\pi^2} \int d\Omega \rho(\mathbf{r}, \Omega). \end{aligned} \quad (6)$$

By definition,  $\rho^0$  and  $\rho^1$  satisfy

$$\int d\mathbf{r} \rho^0(\mathbf{r}) = \frac{N}{8\pi^2}, \quad (7)$$

$$\int d\Omega \rho^1(\mathbf{r}, \Omega) = 0. \quad (8)$$

The latter constraint follows from the properties of the  $D_{lmn}$ .<sup>21</sup>

For convenience, two additional functions are defined in terms of  $\rho^0$  and  $\rho^1$ . The first is the orientation-independent number density, given by

$$c(\mathbf{r}) \equiv \int d\Omega \rho(\mathbf{r}, \Omega) = 8\pi^2 \rho^0(\mathbf{r}). \quad (9)$$

It is equivalent to the number density used when molecular orientation is not taken into account, such as in equations of state, for example. The second function is the normalized orientational probability density, defined by

$$\hat{f}(\mathbf{r}, \Omega) \equiv \frac{\rho(\mathbf{r}, \Omega)}{c(\mathbf{r})} = \hat{f}_0 \left( 1 + \frac{\rho^1(\mathbf{r}, \Omega)}{\rho^0(\mathbf{r})} \right), \quad (10)$$

where  $\hat{f}_0 = 1/(8\pi^2)$  is the orientational probability density in an isotropic medium. These two functions satisfy the constraints

$$\int d\mathbf{r} c(\mathbf{r}) = N, \quad (11)$$

$$\int d\Omega \hat{f}(\mathbf{r}, \Omega) = 1. \quad (12)$$

### B. Helmholtz free energy

In terms of  $\rho^0$  and  $\rho^1$ , the Helmholtz free energy is given by

$$F[\rho^0, \rho^1] = E[\rho^0, \rho^1] - TS[\rho^0, \rho^1], \quad (13)$$

where  $E$  is the internal energy of the system,  $T$  its temperature, and  $S$  its entropy. While  $E$  includes terms that might favor some orientational order,  $S$  always favors a state of no order.

Assuming that  $E$  can be expanded as a series about the isotropic state, it is written as

$$\begin{aligned} E[\rho^0, \rho^1] &= E_0[\rho^0] + \sum_{l=1}^{\infty} \frac{1}{l!} \int d\mathbf{r}_1 d\Omega_1 \cdots d\mathbf{r}_l d\Omega_l \\ &\quad \times \Phi_l[\mathbf{r}_1, \Omega_1, \dots, \mathbf{r}_l, \Omega_l; \rho^0] \\ &\quad \times \rho^1(\mathbf{r}_1, \Omega_1) \cdots \rho^1(\mathbf{r}_l, \Omega_l), \end{aligned} \quad (14)$$

where

$$\Phi_l[\mathbf{r}_1, \Omega_1, \dots, \mathbf{r}_l, \Omega_l; \rho^0] \equiv \left( \frac{\delta^l E}{\delta \rho(\mathbf{r}_1, \Omega_1) \cdots \delta \rho(\mathbf{r}_l, \Omega_l)} \right)_{\rho^0}. \quad (15)$$

The functional derivatives are evaluated at the isotropic state. For cases where the major contribution to the free energy comes from the isotropic term, a truncated expansion is sufficient to capture the phenomena of interest. As will be seen in Sec. III, this assumption is valid for water.

The entropy term, on the other hand, is divided into two parts:

$$S[\rho^0, \rho^1] = S_0[\rho^0] + \Delta S[\rho^0, \rho^1], \quad (16)$$

where  $S_0$  is the entropy of the isotropic medium and  $\Delta S$  is the excess entropy due to anisotropy. The formula for  $\Delta S$  is derived by noting that the excess entropy density,  $s(\mathbf{r})$ , at a point  $\mathbf{r}$  in space is given by

$$\begin{aligned} s(\mathbf{r}) &\equiv -R \left( \int d\Omega \hat{f}(\mathbf{r}, \Omega) \ln \hat{f}(\mathbf{r}, \Omega) - \int d\Omega \hat{f}_0 \ln \hat{f}_0 \right) \\ &= -R \left( \int d\Omega \hat{f}(\mathbf{r}, \Omega) \ln \hat{f}(\mathbf{r}, \Omega) - \int d\Omega \hat{f}(\mathbf{r}, \Omega) \ln \hat{f}_0 \right) \\ &= -R \left( \int d\Omega \hat{f}(\mathbf{r}, \Omega) \ln \frac{\hat{f}(\mathbf{r}, \Omega)}{\hat{f}_0} \right). \end{aligned} \quad (17)$$

The total excess entropy in the system is the weighted integral of  $s$  over the whole system:

$$\begin{aligned} \Delta S[\rho^0, \rho^1] &\equiv \int d\mathbf{r} c(\mathbf{r}) s(\mathbf{r}) \\ &= -R \int d\mathbf{r} d\Omega (\rho^0(\mathbf{r}) \\ &\quad + \rho^1(\mathbf{r}, \Omega)) \ln \left( 1 + \frac{\rho^1(\mathbf{r}, \Omega)}{\rho^0(\mathbf{r})} \right). \end{aligned} \quad (18)$$

Inserting the expressions for  $E$  and  $S$  from Eqs. (14), (16), and (18) into Eq. (13), the Helmholtz free energy is given by

$$\begin{aligned} F[\rho^0, \rho^1] &= F_0[\rho^0] + RT \int d\mathbf{r} d\Omega (\rho^0(\mathbf{r}) + \rho^1(\mathbf{r}, \Omega)) \\ &\quad \times \ln \left( 1 + \frac{\rho^1(\mathbf{r}, \Omega)}{\rho^0(\mathbf{r})} \right) + \sum_{l=1}^{\infty} \frac{1}{l!} \int d\mathbf{r}_1 d\Omega_1 \cdots d\mathbf{r}_l d\Omega_l \\ &\quad \times \Phi_l[\mathbf{r}_1, \Omega_1, \dots, \mathbf{r}_l, \Omega_l; \rho^0] \\ &\quad \times \rho^1(\mathbf{r}_1, \Omega_1) \cdots \rho^1(\mathbf{r}_l, \Omega_l), \end{aligned} \quad (19)$$

where

$$F_0[\rho^0] = E_0[\rho^0] - TS_0[\rho^0]. \quad (20)$$

The first term in the expansion,  $F_0$ , is the only term that survives when the medium is isotropic. For water, it consists of a classical part (see Sec. III A) plus a gradient correction that accounts for the finite width of interfaces (see Sec. III B). The other terms in the expansion are kernel-type integrals of powers of  $\rho^1$ . The first order term, for example, can be thought of as an external potential-like term. The second order term, on the other hand, has two-body interaction character. In general, the  $n$ th-order term involves an  $n$ -body interaction-like kernel. As explained in Sec. III C, an expansion up to first order appears to be sufficient to capture interfacial water orientation phenomena.

Although the above formalism has been developed with water in mind, it is general and applies to any structured fluid. A ferromagnetic-like phenomenon, induced by the second order term, is presented elsewhere.<sup>22</sup> There, the degree of ordering in the homogeneous bulk is studied as a function of interaction strength. This example was also used to verify our numerical approach by comparing numerical results with the analytical results that are obtained via a bifurcation analysis.

### C. Free energy minimization

The mesoscopic structures of interest arise from the minimization of  $F$  with respect to  $\rho^0$  and  $\rho^1$ , subject to the constraints in Eqs. (7) and (8), respectively. Using the method of Lagrange multipliers, an auxiliary functional

$$\begin{aligned} \tilde{F}[\rho^0, \rho^1] &\equiv F[\rho^0, \rho^1] - \bar{\mu} \left( \int d\mathbf{r} 8\pi^2 \rho^0(\mathbf{r}) - N \right) \\ &\quad - \int d\mathbf{r} \lambda(\mathbf{r}) \int d\Omega \rho^1(\mathbf{r}, \Omega) \end{aligned} \quad (21)$$

is defined. In this equation,  $\bar{\mu}$  is a Lagrange multiplier associated with the mass conservation constraint [Eq. (7)], while  $\lambda(\mathbf{r})$  is a Lagrange multiplier function associated with the constraint on  $\rho^1$  [Eq. (8)]. Setting the functional derivatives of  $\tilde{F}$  to zero, the equilibrium conditions are given by

$$\frac{\delta F}{\delta \rho^0(\mathbf{r})} = 8\pi^2 \bar{\mu}, \quad (22)$$

$$\frac{\delta F}{\delta \rho^1(\mathbf{r}, \Omega)} = \lambda(\mathbf{r}). \quad (23)$$

Solving Eqs. (22) and (23) locates a stationary point of  $\tilde{F}$ . This point could be a minimum, a maximum or a saddle point. To drive the system to a *minimum* of the free energy that satisfies the constraints in Eqs. (7) and (8), the descriptive variables are evolved along the path generated by

$$\frac{\partial \rho^0(\mathbf{r})}{\partial t} = -q_0 \left\{ \frac{\delta F}{\delta \rho^0(\mathbf{r})} - 8\pi^2 \bar{\mu} \right\}, \quad (24)$$

$$\frac{\partial \rho^1(\mathbf{r}, \Omega)}{\partial t} = -q_1 \left\{ \frac{\delta F}{\delta \rho^1(\mathbf{r}, \Omega)} - \lambda(\mathbf{r}) \right\}, \quad (25)$$

where  $t$  is a pseudo-time variable and  $q_0$  and  $q_1$  are positive proportionality constants. This scheme is a generalization of the method of steepest descent,<sup>23</sup> which is a local minimization algorithm.

In order to determine  $\rho^0$  and  $\rho^1$  through Eqs. (24) and (25), one needs the values of the Lagrange multipliers. The direct method of solving for the variables in terms of the Lagrange multipliers and then solving a set of equations for the latter is not practical in this case. Since the densities cannot be written as explicit functions of the Lagrange multipliers, one must solve for both the densities and the Lagrange multipliers iteratively, which is very time consuming.

Alternatively,<sup>24</sup> integrating Eq. (24) over the system volume and applying the mass conservation constraint to the left-hand side, it is found that

$$0 = \int d\mathbf{r} \frac{\delta F}{\delta \rho^0(\mathbf{r})} - 8\pi^2 V \bar{\mu}, \quad (26)$$

where  $V$  is the volume of the system. Thus, for given  $\rho^0$  and  $\rho^1$ ,  $\bar{\mu}$  is obtained from

$$\bar{\mu} = \frac{1}{8\pi^2 V} \int d\mathbf{r} \frac{\delta F}{\delta \rho^0(\mathbf{r})}. \quad (27)$$

Similarly, integrating Eq. (25) over all solid angles and applying the constraint in Eq. (8) to the left-hand side yields

$$\lambda(\mathbf{r}) = \frac{1}{8\pi^2} \int d\Omega \frac{\delta F}{\delta \rho^1(\mathbf{r}, \Omega)}. \quad (28)$$

Using Eqs. (27) and (28), the Lagrange multipliers are evolved in time along with  $\rho^0$  and  $\rho^1$  until a minimum is reached.

#### D. Numerical techniques

Due to the complexity of Eqs. (24), (25), (27), and (28), they are solved using numerical methods. Equations (24) and (25) are partial integrodifferential equations that involve derivatives with respect to time and space. They constitute an initial boundary value problem, solved for specified initial data and boundary conditions. Neumann boundary conditions are used because they do not introduce boundary artifacts. The initial data is chosen to be in the basin of attraction of the minimum of interest, and it satisfies both boundary conditions and constraints.

Spatial and angular discretization is achieved through a combination of the finite element<sup>25</sup> and the finite difference<sup>23</sup> methods. The former is superior for solving partial differential equations over domains with complex geometry, and thus the overall problem is cast in a finite element formulation. Both space and angular degrees of freedom are divided into hexahedral elements. Using an isoparametric formulation, element geometry and the value of the dependent variables inside each element are interpolated using linear approximation functions of the Lagrange family. Numerical integration is performed using Gauss–Legendre quadrature.<sup>25</sup> Since linear interpolation functions are used, second partial derivatives of the dependent variables cannot be accurately evaluated using the finite element method. Thus the first and second partial derivatives of  $c$  in  $\Phi_1$  [Eq. (36)] and  $\delta\Phi_1/\delta c$  are conveniently evaluated using a second order finite difference approximation.

Discretizing Eqs. (24) and (25) with respect to space and angles converts them into a set of ordinary differential equations in the values of  $\rho^0$  and  $\rho^1$  at the interpolation nodes. The “time” variable in these equations is then discretized using a first order, mixed explicit/implicit scheme, where the time step is allowed to adapt dynamically to the nature of the equations. For stability purposes, the Laplacian term in the free energy (see Sec. III B) is treated implicitly. For efficiency, the rest of the terms—which are nonlinear—are integrated explicitly in time. The overall discretized problem is then solved using a preconditioned conjugate gradient method.<sup>26</sup>

### III. FREE ENERGY OF WATER

#### A. Classical equation of state

The classical equation of state used in our model is that developed by Jeffery and Austin.<sup>27</sup> It involves a “bulk” part as well as an explicit contribution from strong hydrogen bonding, which is important to model the anomalous behavior of water below 4 °C at atmospheric pressure.

Dividing the intermolecular interaction potential into a dominant repulsive term and a much weaker attractive term, their “bulk” equation of state is given by

$$\frac{p}{cRT} = 1 - b^*c - \frac{a_{vw}c}{RT} + \frac{\alpha c}{1 - \lambda b(T)c}, \quad (29)$$

where  $p$  is the pressure,  $c$  the number density defined in the previous section,  $T$  the temperature, and  $R$  the gas constant. The second and third terms on the right-hand side account for the entropy and energy, respectively, of the attractive part of the interaction between two water molecules. The fourth term arises from the hard sphere model of the repulsive part of the interaction.

The explicit contribution from strong hydrogen bonds, in the form of a free energy density, is approximated by the expression

$$f_{\text{HB}}(c) = -2fcRT \ln[\Omega_0 + \Omega_{\text{HB}} \exp(-\epsilon_{\text{HB}}/RT)] - 2(1-f)cRT \ln[\Omega_0 + \Omega_{\text{HB}}], \quad (30)$$

where  $\Omega_0$  is the number of configurations of weak hydrogen bonds with energy 0,  $\Omega_{\text{HB}}$  is the number of configurations of strong, tetrahedral hydrogen bonds with energy  $\epsilon_{\text{HB}}$ , and  $f$  is the fraction of hydrogen bonds that are capable of forming strong bonds.

Combining the two contributions, the classical free energy density of water in our model is given by

$$f_{\text{cl}} = f_{\text{eos}} + f_{\text{HB}}. \quad (31)$$

The “bulk” free energy density is derived from the “bulk” equation of state [Eq. (29)] using<sup>28</sup>

$$f_{\text{eos}}(c) = c \int_0^c \frac{p(c')}{c'^2} dc'. \quad (32)$$

This analytic equation of state is 20–30 times more accurate than equivalent simple cubic equations in the temperature range –34 to 1200 °C and pressures up to 3000 bar.<sup>27</sup>

Using their equation of state, the liquid and vapor densities that coexist at equilibrium at  $T=300$  K, which is the temperature of interest to us, are  $c_l=55165.7$  mol/m<sup>3</sup> and  $c_v=17.14$  mol/m<sup>3</sup>, respectively. Bulk liquid and bulk vapor at these densities have the same chemical potential and pressure.

#### B. Gradient correction

The classical equation of state introduced in the previous section includes no correlation between the concentration at different points in space. Thus, for example, the concentration at one point can be that of liquid water while it is that of water vapor at a point an infinitesimal distance away. As a result, interfaces between different phases have no width. Although unphysical, this approximation is acceptable in macroscopic systems where the length scales of interest are much larger than the width of an interface.

In mesoscopic systems, however, the characteristic lengthscale of many interactions is comparable to the width of the water–vapor interface. Figure 2 is a schematic depiction of a hydrophobic site on a molecule immersed in water. We hypothesize that the local hydrophobicity induces a low water density region, the properties of which change gradually to those of bulk liquid. Thus the atoms at this site interact most strongly with water molecules in the “vapor” phase, followed by those in the interface, followed by those in the liquid region. None of these three regions is negligible.

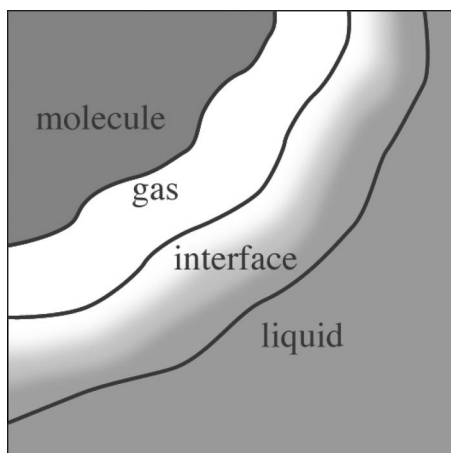


FIG. 2. Schematic depiction of a molecule with a hydrophobic site immersed in water, suggesting that it creates a “vapor”–liquid interface.

One way to include spatial correlation of descriptive variables, such as the concentration in our model, is by using gradient terms. The first to introduce such a correction in his study of interfaces appears to be van der Waals in 1893.<sup>29</sup> He used a term similar to the one used in our model, described below. Related classical density functional approaches are found in Refs. 30–36, and references therein.

Gradient terms vanish for uniform systems, since, by construction, the classical term is sufficient in that case. Also, in order to model the liquid–vapor interface of water, they must be always positive for nonuniform systems. The latter condition must be satisfied by the gradient correction because otherwise it will be energetically favorable to form interfaces and the system would evolve toward ever-increasing interfacial surface areas.

The simplest form of a gradient correction to the free energy density is given by

$$f_{\text{grad}}(c(\mathbf{r})) = \frac{1}{2} \Lambda(c(\mathbf{r}), T) |\nabla c(\mathbf{r})|^2, \quad (33)$$

where  $\Lambda(c(\mathbf{r}), T)$  is a phenomenological parameter that depends on concentration and temperature. As a first step, we

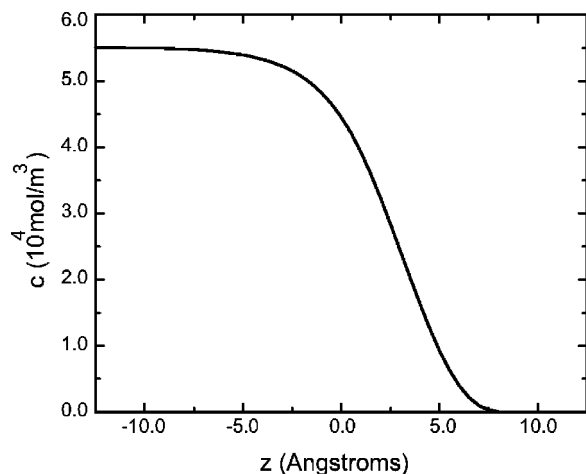


FIG. 3. 7.5 Å planar water–vapor interface obtained by minimizing a free energy that consists of the classical equation of state of Sec. III A and a gradient correction with  $\Lambda = 4.3 \times 10^{-20} \text{ J m}^5/\text{mol}^2$ .

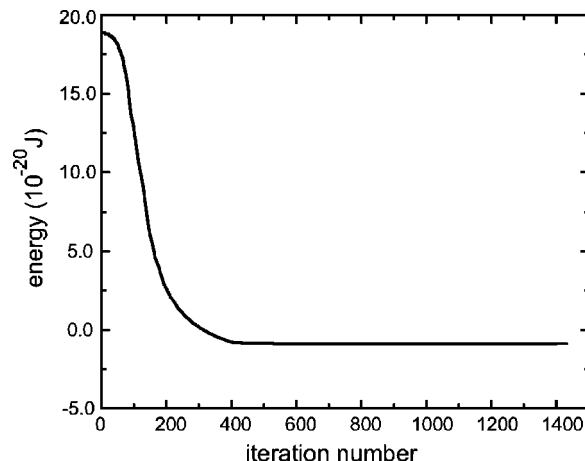


FIG. 4. System free energy vs iteration number in the isotropic planar interface simulation discussed in Sec. III B.

assume here that  $\Lambda$  is a function of temperature only. Since we are interested in phenomena that take place at room temperature and pressure, its value is determined such that it yields a 10%–90% width of about 7.5 Å for the water–vapor interface at 300 K. This value is a reasonable starting point since the value measured experimentally ranges between 6.7 Å (Ref. 37) and 8 Å.<sup>38</sup>

Figure 3 shows a planar water–vapor interface obtained by minimizing  $F_0$  with respect to  $\rho^0$  subject to the mass conservation constraint [Eq. (7)], using  $\Lambda = 4.3 \times 10^{-20} \text{ J m}^5/\text{mol}^2$ . The initial concentration profile had bulk liquid in the lower half of the system and bulk vapor in the upper half of the system. In this simulation, we use 50  $0.5 \text{ Å}$  finite elements in the  $z$  direction. Figure 4 shows the decrease of the free energy of the system during the simulation.

### C. Anisotropic term

The third contribution to the free energy needed to model orientational structure at an interface is the first-order anisotropic term. Thus the expansion of  $F$  [Eq. (19)] is truncated to first-order, retaining the external-potential-like term. It seems to be sufficient to model orientation at a planar interface, and, since order at a droplet’s surface is observed to be independent of its size,<sup>8,9</sup> it should be sufficient to model orientation at curved interfaces as well.

In order to induce orientation through spatial gradients of the density, the kernel,  $\Phi_1[\mathbf{r}, \Omega; \rho^0]$ , is written as an interaction between  $\nabla c$  and the two perpendicular vectors  $\hat{\mathbf{n}}$  and  $\hat{\mathbf{m}}$  defined in Fig. 5. The vectors  $\hat{\mathbf{n}}$  and  $\hat{\mathbf{m}}$  are, respec-

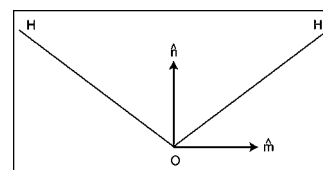


FIG. 5. Definition of unit vectors  $\hat{\mathbf{n}}$  and  $\hat{\mathbf{m}}$ , where  $\hat{\mathbf{n}}$  specifies the direction of the dipole moment of the water molecule, while both vectors define the molecular plane.

tively, equivalent to  $\hat{\mathbf{z}}_b$  and  $\hat{\mathbf{x}}_b$  of Fig. 1. In terms of the Euler angles, they are given by

$$\hat{\mathbf{n}} = \sin \theta \cos \phi \hat{\mathbf{x}} + \sin \theta \sin \phi \hat{\mathbf{y}} + \cos \theta \hat{\mathbf{z}}, \quad (34)$$

$$\hat{\mathbf{m}} = (-\sin \chi \sin \phi + \cos \theta \cos \phi \cos \chi) \hat{\mathbf{x}} + (\sin \chi \cos \phi + \cos \theta \sin \phi \cos \chi) \hat{\mathbf{y}} - \cos \chi \sin \theta \hat{\mathbf{z}}. \quad (35)$$

The simplest form for  $\Phi_1$  that is rich enough to capture the orientational order of water molecules at the interface can be written as

$$\Phi_1[\mathbf{r}, \Omega; c] = \lambda_1(c(\mathbf{r})) |\nabla c(\mathbf{r})|^2 \nabla c(\mathbf{r}) \cdot \hat{\mathbf{n}} + \lambda_2(c(\mathbf{r})) \times (\nabla c(\mathbf{r}) \cdot \hat{\mathbf{n}})^2 + \lambda_3(c(\mathbf{r})) (\nabla c(\mathbf{r}) \cdot \hat{\mathbf{m}})^2, \quad (36)$$

where  $c$  is being used instead of  $\rho^0$ . Among the  $\hat{\mathbf{n}}$ -dependent terms, the first favors an angle of  $180^\circ$  between  $\hat{\mathbf{n}}$  and the gradient when  $\lambda_1 > 0$  and an angle of  $0^\circ$  when  $\lambda_1 < 0$ . The second term has a minimum at  $90^\circ$  when  $\lambda_2 > 0$  and two minima at  $0^\circ$  and  $180^\circ$  when  $\lambda_2 < 0$ . Thus a balance between the first and second terms yields the desired angle between  $\nabla c$  and  $\hat{\mathbf{n}}$ . The last term in Eq. (36) depends on the vector  $\hat{\mathbf{m}}$ , and, given a certain alignment for  $\hat{\mathbf{n}}$ , determines the orientation of the molecular plane with respect to the interface. It is symmetrical with respect to inversion of  $\hat{\mathbf{m}}$ , as required by the symmetry of the water molecule. As with the second term,  $\lambda_3 > 0$  favors  $\hat{\mathbf{m}}$  to be perpendicular to  $\nabla c$ , while  $\lambda_3 < 0$  prefers parallel or antiparallel alignment.

For illustrative purposes, before calibrating the model to reproduce the results of molecular dynamics simulations of the liquid-vapor interface of water,<sup>7</sup> let  $\lambda_1$  and  $\lambda_2$  be zero while  $\lambda_3$  is given by

$$\lambda_3 = 3 \times 10^{-5} \tanh(5(c - c_G)), \quad (37)$$

in units of  $(\text{J/mol}) \times (\text{mol/m}^3/\text{\AA}^2)$ . A hyperbolic tangent is used to obtain a smooth transition between the behavior on the liquid side and that on the vapor side of the interface. The concentration,  $c_G$ , at which  $\lambda_3$  changes its sign is that at the Gibbs dividing plane in a planar liquid-vapor interface. Assuming that the interface is normal to the  $z$ -axis, the Gibbs dividing plane is defined to be at  $z_G$  given by<sup>7,30</sup>

$$\int_{-\infty}^{z_G} (c(z) - c_l) dz = - \int_{z_G}^{\infty} (c(z) - c_v) dz, \quad (38)$$

where  $c_v$  and  $c_l$  are defined in Sec. III A. It is found that  $c_G \approx 30785 \text{ mol/m}^3$  under the model developed in Secs. III A and III B.

From the form of  $\lambda_3$ ,  $\Phi_1$  has the same strength on both sides of the interface, but the coefficient is positive in the liquid and negative in the vapor. Thus it is energetically favorable to have  $\hat{\mathbf{m}}$  perpendicular to  $\nabla c$  (i.e., parallel to the interface) on the liquid side and parallel or antiparallel to  $\nabla c$  (i.e., perpendicular to the interface) on the vapor side.

The results of simulating order at a planar interface, where the concentration gradient is along the  $z$ -axis and where there is no dependence on  $x$ ,  $y$  and  $\phi$ , are shown in Figs. 6–8. Initially,  $\rho^0$  is given by the concentration profile in Fig. 3 while  $\rho^1$  is taken to be zero everywhere. The same number of spatial elements as in the isotropic case above was

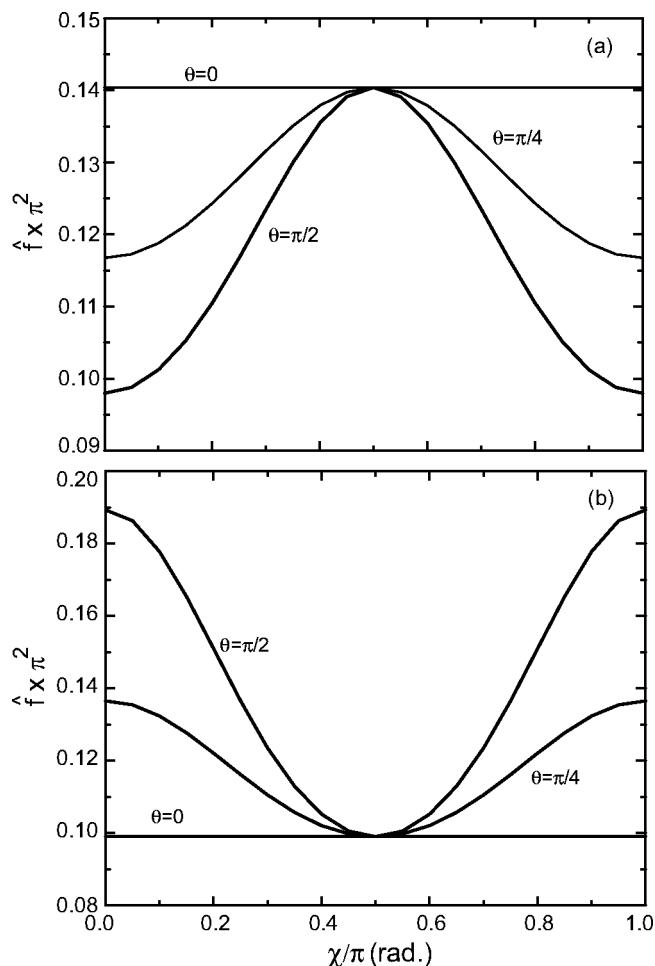


FIG. 6. Free energy minimizing orientational probability density,  $\hat{f}$ , as a function of  $\chi$  at several  $\theta$  values in the case where  $\Phi_1$  is given by Eqs. (36) and (37), (a) on the liquid side and (b) on the vapor side of the planar liquid-vapor interface of water.

used. The  $\theta$  and  $\phi$  directions were divided into elements of  $0.05\pi$  each, while only one element was used for  $\phi$  since there is no dependence on it.

Figure 6 shows  $\hat{f}$  as a function of  $\chi$  for several values of  $\theta$  averaged over a  $3 \text{ \AA}$  slab on the liquid side and a  $3 \text{ \AA}$  slab on the vapor side of the Gibbs dividing plane. Due to the symmetry of the water molecule, any function of  $\chi$  satisfies  $f(\chi + \pi) = f(\chi)$  and thus it suffices to plot  $\hat{f}$  for  $\chi$  between  $0$  and  $\pi$  only. It is seen from the two graphs that all values of  $\chi$  are equally likely when  $\hat{\mathbf{n}}$  is perpendicular to the interface ( $\theta = 0$ ), since  $\hat{\mathbf{m}}$  in this case is parallel to the interface no matter what the value of  $\chi$  is. For  $\theta \neq 0$ , the slab on the liquid side has a maximum at  $\chi = 90^\circ$ , where  $\hat{\mathbf{m}}$  is parallel to the interface, and the slab on the vapor side has maxima at  $\chi = 0^\circ, 180^\circ$  where  $\hat{\mathbf{m}}$  is perpendicular to the interface. The distributions are narrowest for  $\theta = 90^\circ$ .

Figure 7(a) shows  $\hat{f}'$ , defined by

$$\hat{f}'(\mathbf{r}, \theta) = \int_0^{2\pi} d\chi \int_0^{2\pi} d\phi \hat{f}(\mathbf{r}, \Omega), \quad (39)$$

averaged over a  $3 \text{ \AA}$  slab on the liquid side and a  $3 \text{ \AA}$  slab on the vapor side of the Gibbs dividing plane, respectively. The

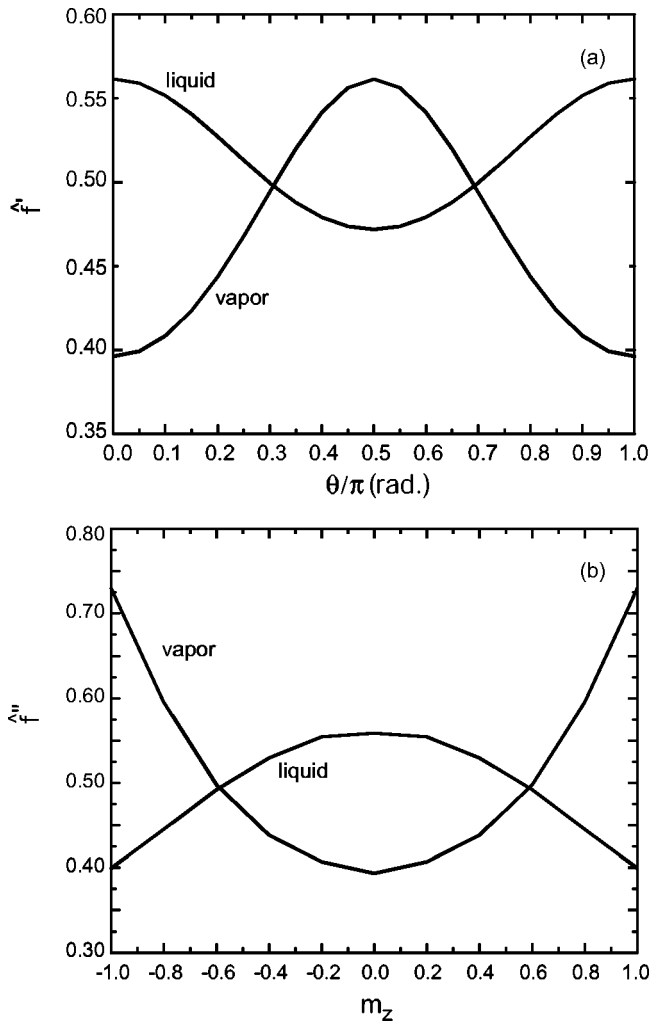


FIG. 7. Free energy minimizing (a)  $\hat{f}'$  [defined in Eq. (39)] as a function of  $\theta$  and (b)  $\hat{f}''$  [defined in Eq. (40)] as a function of  $m_z$  at the planar liquid–vapor interface of water in the case where  $\Phi_1$  is given by Eqs. (36) and (37).

distribution is quite interesting because, although there is no explicit dependence of  $\Phi_1$  on  $\hat{\mathbf{n}}$ , the distribution has a maximum for  $\hat{\mathbf{n}}$  perpendicular to the interface on the liquid side and  $\hat{\mathbf{n}}$  parallel to the interface on the vapor side. This result is expected since when  $\hat{\mathbf{n}}$  is perpendicular to the interface,  $\hat{\mathbf{m}}$  is always parallel to it, which is the energetically favorable orientation on the liquid side. On the vapor side,  $\hat{\mathbf{n}}$  prefers to be in the interface plane because this implies that  $\hat{\mathbf{m}}$  has the highest probability to be perpendicular to the interface

Figure 7(b) shows  $\hat{f}''$ , the probability distribution of  $m_z$ , the  $z$  component of  $\hat{\mathbf{m}}$  defined in Eq. (35), again averaged over 3 Å slabs on both sides of the interface. The normalized probability density, defined by

$$\hat{f}''(\mathbf{r}, m_z) = \int d\Omega \hat{f}(\mathbf{r}, \Omega) \delta(m_z + \sin \theta \cos \chi), \quad (40)$$

is approximated by the integral

$$\hat{f}''(\mathbf{r}, m_z) \approx \int d\Omega \hat{f}(\mathbf{r}, \Omega) A e^{-((m_z + \sin \theta \cos \chi)/a)^2}. \quad (41)$$

The parameter  $a$  is chosen to yield reasonable sampling considering the discretized nature of the numerically computed

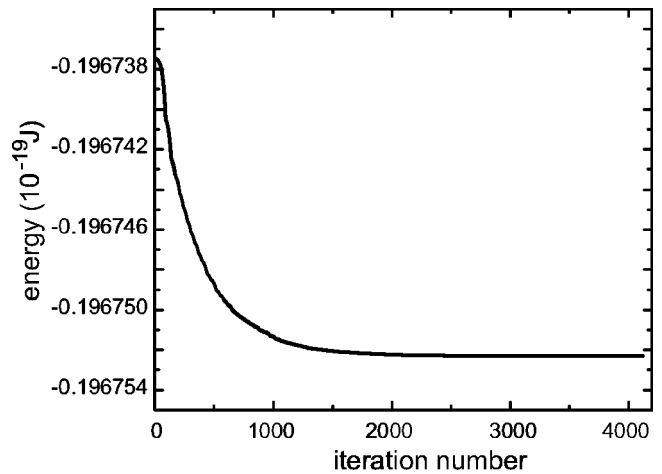


FIG. 8. Energy of system vs iteration number in the simulation of orientational order at the planar liquid–vapor interface of water in the case where  $\Phi_1$  is given by Eqs. (36) and (37).

probability, while the coefficient  $A$  is used to normalize  $\hat{f}''$  to unity. From the graphs, it is seen that  $\hat{f}''$  has a maximum at  $m_z=0$  on the liquid side, and maxima at 1 and  $-1$  on the vapor side, as expected from the form of  $\Phi_1$  and the results presented in Figs. 6 and 7(a).

It is seen from the figures that there is more ordering on the vapor side than on the liquid side of the interface. This is due to the fact that the concentration gradient is larger on the vapor side than on the liquid side, and, as suggested by our model, larger gradients induce more ordering.

The change in the free energy of the system over the course of the minimization is shown in Fig. 8. The absolute magnitude of the orientation-dependent energy term is found to be about four orders of magnitude smaller than  $F_0$ . Since the profile of  $\rho^0$  stays almost the same throughout the simulation, most of the change in the free energy comes from change in  $\rho^1$ , explaining why the change in the total free energy is so small. This difference in magnitude, which is also seen in the case of water molecules below, justifies the expansion in Eq. (19).

Back to the case of water molecules at the liquid–vapor interface, it is seen from molecular dynamics simulations<sup>7</sup> that the dominant feature of the orientation of water molecules at the interface for  $T=298$  K is the almost parallel alignment of their dipole moments to it. This requires the second term in Eq. (36) to be dominant, with  $\lambda_2 > 0$ . Since the dipole moments make a small angle with the interface and point in two different directions on the two sides, the first term should be much weaker than the second one and  $\lambda_1$  must change signs when passing from the liquid side to the vapor side, i.e., at the Gibbs dividing plane. The simulations also show that there is weak preferred orientation of the molecular plane parallel to the interface on the liquid side and perpendicular to it on the vapor side. Thus  $\lambda_3$  should also change signs at  $c_G$ .

These observations are reproduced by the set of values (see Fig. 9)

$$\lambda_1 = -3 \times 10^{-9} \tanh(5(c - c_G)),$$

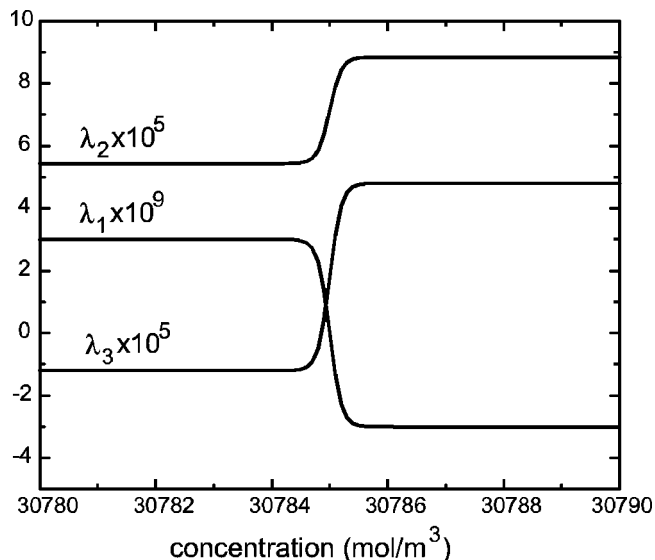


FIG. 9. The coefficients  $\lambda_1$ ,  $\lambda_2$ , and  $\lambda_3$  [given in Eq. (42)] in  $\Phi_1$  used to model water orientation at the liquid–vapor interface.

$$\lambda_2 = 1.7 \times 10^{-5} (\tanh(5(c - c_G)) + 4.2), \quad (42)$$

$$\lambda_3 = 3 \times 10^{-5} (\tanh(5(c - c_G)) + 0.6),$$

where  $\lambda_1$  is in units of  $(\text{J/mol}) \times (\text{mol/m}^3/\text{\AA})^3$  and  $\lambda_2$  and  $\lambda_3$  are in units of  $(\text{J/mol}) \times (\text{mol/m}^3/\text{\AA})^2$ . The results of using these values in simulating orientational order at a planar interface with initial data and numerical details like those in the previous example (except that the  $\theta$  direction is divided into twice as many elements) are shown in Figs. 10–12. Figure 10 shows the profile of  $c$  at the beginning and the end of the simulation, which are found to be very close to each other. The free energy of the system throughout the simulation is shown in Fig. 11. The probability distributions of  $\theta, \hat{f}'$  defined in Eq. (39), averaged over 3  $\text{\AA}$  slabs on both sides of

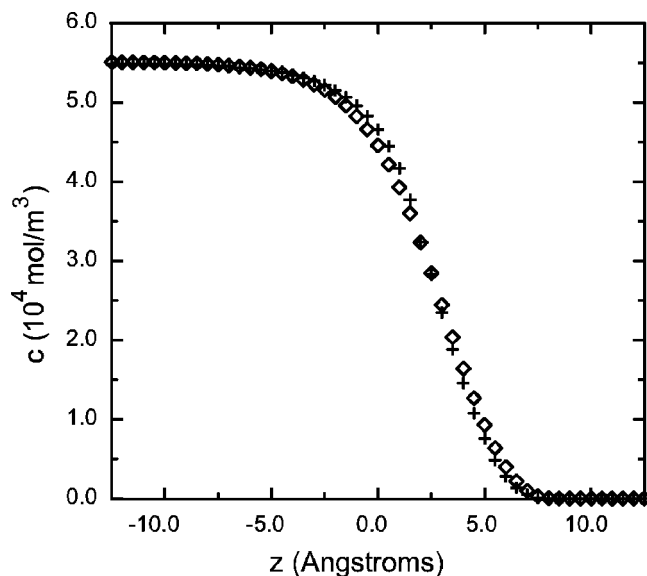


FIG. 10. Initial (diamonds) and final (+) concentration profiles for the planar liquid–vapor interface of water in a free energy minimization simulation where  $\Phi_1$  is given by Eqs. (36) and (42).

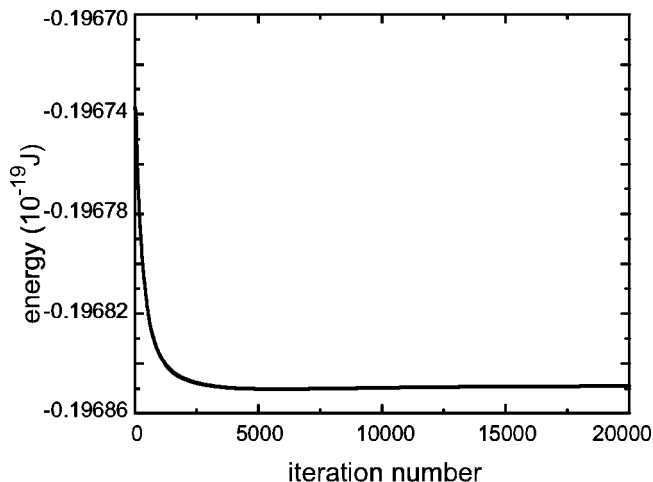


FIG. 11. System free energy vs iteration number for simulation of the planar liquid–vapor interface of water with  $\Phi_1$  given by Eqs. (36) and (42). The slight rise in free energy is a result of small numerical error.

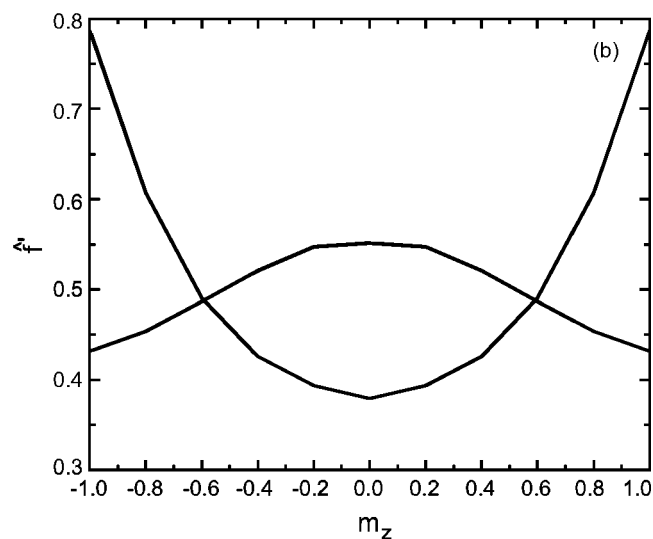
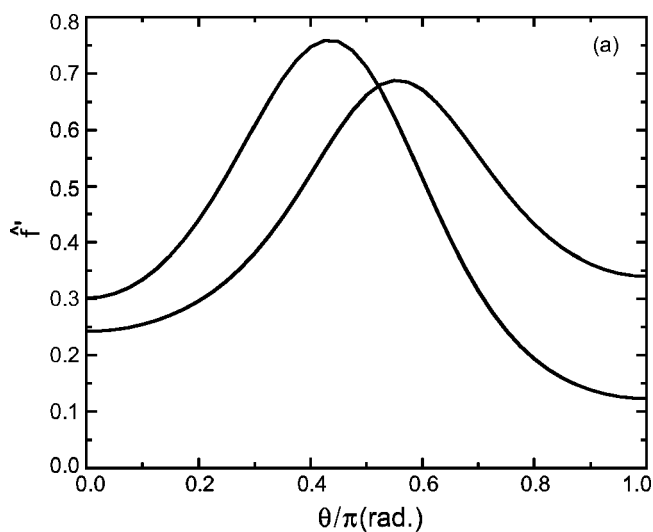


FIG. 12. Free energy minimizing (a)  $\hat{f}'$  [defined in Eq. (39)] as a function of  $\theta$  and (b)  $\hat{f}''$  [defined in Eq. (40)] as a function of  $m_z$  at the planar liquid–vapor interface of water with  $\Phi_1$  given by Eqs. (36) and (42).

the interface are shown in Fig. 12(a). The distributions have maxima at about  $99^\circ$  on the liquid side and about  $77^\circ$  on the vapor side. The distribution of  $m_z$ , i.e.,  $\hat{f}''$  [defined in Eq. (40)] averaged over 3 Å slabs on both sides of the interface, shown in Fig. 12(b), indicates that a majority of water molecules has  $m_z$  parallel to the interface on the liquid side and perpendicular to it on the vapor side. Combining these distributions with those of  $\theta$  implies that most molecules have their plane parallel to the interface on the liquid side and perpendicular to it on the vapor side.

The above results agree well with the molecular dynamics results used to calibrate the model.<sup>7</sup> The locations and heights of the distributions' maxima are very close to what is presented there.

## IV. RESULTS AND DISCUSSION

### A. Surface tension of a planar interface

The formation of an interface between two phases has a free energy cost whose value per unit area is defined as the surface tension of the interface. Since, as seen above, the anisotropic term in the free energy is about four orders of magnitude smaller than  $F_0$ , the major contribution to the surface tension comes from the equation of state and gradient terms.

In our model, retaining only  $F_0$ , the surface tension of a planar interface normal to the  $z$ -axis is given by<sup>30,36</sup>

$$\gamma = \Lambda \int_{-\infty}^{\infty} dz \left( \frac{dc}{dz} \right)^2. \quad (43)$$

As determined in Sec. III B, taking  $\Lambda = 4.3 \times 10^{-20}$  J m<sup>5</sup>/mol<sup>2</sup> and using the free energy minimizing concentration profile in Fig. 3, it is found that  $\gamma \approx 135$  mN/m. Experimentally, the surface tension is measured to be about 72 mN/m at 300 K,<sup>39</sup> and thus our result is about twice the observed value. This discrepancy is most probably due to the simplicity of the gradient correction used.

Better values for the surface tension can be obtained by using an expression for  $\Lambda$  that is a function of concentration and that involves two parameters that are calibrated to match both the interface width and the surface tension. One can also use other gradient terms in the correction, such as  $|\nabla c|^4$ , for example. We have limited this study to the form in Eq. (33) with a constant  $\Lambda$  as we are mainly concerned with the *orientation* of water molecules at the liquid–vapor interface.

### B. Surface potential of a planar interface

The net orientation of water molecules in the liquid–vapor interface causes a layering of their charge density, producing an electric field. The surface potential thus measures the work performed in moving a test charge from the vapor phase to the liquid phase, across this field. An expression for the surface potential,  $\Delta\phi$ , is<sup>7,12,40</sup>

$$\begin{aligned} \Delta\phi &\equiv \phi(-\infty) - \phi(\infty) \\ &= \int_{-\infty}^{\infty} E_z(z) dz \\ &= -\frac{1}{\epsilon_0} \int_{-\infty}^{\infty} P_z(z) dz - \frac{1}{\epsilon_0} [Q_{zz}(-\infty) - Q_{zz}(\infty)], \end{aligned} \quad (44)$$

where  $P_z$  is the  $z$ -component of the molecular dipole density and  $Q_{zz}$  is the  $zz$ -component of the molecular quadrupole density. They are given by

$$\begin{aligned} P_z(z) &= \left\langle \sum_m \delta(z - z_m) \left[ \sum_j q_{mj} z_{mj} \right] \right\rangle \\ &= c(z) \langle P_z(\Omega) \rangle_{\hat{f}, z}, \end{aligned} \quad (45)$$

$$\begin{aligned} Q_{zz}(z) &= \left\langle \sum_m \delta(z - z_m) \left( \frac{1}{2} \sum_j q_{mj} z_{mj}^2 \right) \right\rangle \\ &= c(z) \langle Q_{zz}(\Omega) \rangle_{\hat{f}, z}, \end{aligned} \quad (46)$$

where the sum over  $m$  goes over all molecules in the system, the sum over  $j$  goes over all atoms in a molecule,  $q_{mj}$  is the charge of the  $j$ th atom in the  $m$ th molecule,  $z_m$  is the space-fixed  $z$  coordinate of the position of the center of the  $m$ th molecule about which the multipoles are evaluated, and  $z_{mj}$  is the space-fixed  $z$  component of the position of the  $j$ th atom in the  $m$ th molecule. The quadrupole moment defined in Eq. (46) is not the conventional quadrupole moment of zero trace, but has a finite trace. The angle brackets  $\langle \dots \rangle$  denote ensemble averaging of microscopic variables and  $\langle \dots \rangle_{\hat{f}, z}$  indicate an averaging over the Euler angles

$$\langle \dots \rangle_{\hat{f}, z} \equiv \int_{\Omega} d\Omega \dots \hat{f}(z, \Omega). \quad (47)$$

Since  $P_z$  is proportional to  $\langle \cos \theta \rangle$ , its contribution is limited to within the interface region, where there is preferential orientation. It is thus a reflection of the degree and type of ordering at the interface. On the other hand, the quadrupole moment contributes through its values in the two bulk phases far from the interface and hence does not yield any information about the interface region. In fact,  $Q_{zz}(\pm\infty) = c(\pm\infty) \times \frac{1}{3} N_A Q$ , where  $Q$  is the trace of the quadrupole tensor of the water molecule and  $N_A$  is Avogadro's number.

Equation (44) is thought to be exact because all higher multipole moments enter it through their derivatives which vanish at  $\pm\infty$  since both limits correspond to translationally invariant phases. A controversial point, however, is the dependence of Eq. (44) on the point in the molecule about which the multipole expansion is performed. Since the water molecule is neutral, its dipole moment is independent of the chosen molecular center. However, the quadrupole moment does depend on it. Thus different values for the surface potential are obtained depending on the choice of molecular center, which seems to contradict its exactness.

Nevertheless, as this equation is commonly used to compute the surface potential, we use it to compare the prediction of our model to those of others. Since our model is calibrated to reproduce data obtained through molecular dy-

namics simulations that use the SPC/E model,<sup>16</sup> we use this model to obtain the dipole and quadrupole moments of the water molecule, whose values are found to be  $\mu = 7.83 \times 10^{-30}$  C m and  $Q = 6.78 \times 10^{-40}$  C m<sup>2</sup> (taking the molecular center to be at the position of the oxygen atom). Using Eq. (44), the surface potential is found to be  $-0.758$  V. It is different from the value obtained in the molecular dynamics simulations<sup>7</sup> since, in our simulations, the density profile and width of the interface are different from theirs. Furthermore, the orientational probability density obtained in our simulations is slightly different from theirs.

However, it is in qualitative agreement with the results of others.<sup>7</sup> As seen from Table IV in the aforementioned reference, values of  $\Delta\Phi$  obtained using different water models vary in magnitude, but they are all negative with an absolute value less than 1 V. As noted there, it is difficult to compare values of the surface potential obtained theoretically to values obtained experimentally. This is because, in electrochemical experiments, electrostatic and chemical contributions to the surface potential are difficult to separate and because these experiments deal with dilute electrolytes which are different from a pure solvent.<sup>7</sup>

One source of error in our calculations—and those of others—is the use of a nonpolarizable water model, where the charge distribution in a water molecule is assumed to be that suitable for the liquid state. In reality, the charge distribution in a water molecule, and thus its multipole moments, depend on the environment surrounding it. However, since the concentration of water molecules on the vapor side is almost negligible compared to that on the liquid side, this error is likely not very significant. Another, probably less significant, source of error in all of these models is the assumption that water molecules are rigid.

### C. Isotropic droplets

Equilibrium droplets of several sizes at  $T = 300$  K were simulated by minimizing  $F_0$  with respect to  $\rho^0$ , starting with profiles that had liquid density at the center which gradually decayed to that of vapor at the boundary. Cubic elements of  $1 \text{ \AA}$  sides were used to discretize space. Care had been taken to have enough vapor surrounding the droplets so that finite system size effects were minimized. Some runs were repeated using a much larger system, i.e., with more vapor around the droplets, and the results were found to be the same. The final, free energy minimizing droplets had radii ranging from  $13 \text{ \AA}$  (about 300 water molecules) to  $91 \text{ \AA}$  (about  $10^5$  water molecules). A typical droplet (of radius  $28 \text{ \AA}$ ) is shown in Fig. 13. The energy of the system throughout this simulation is shown in Fig. 14.

It is observed that droplets with a smaller radius have a density higher than that of bulk liquid in the middle. As the radius gets larger, the density goes to that of infinite bulk liquid. Similarly, the density of the vapor surrounding smaller droplets is quite high, and it goes to that of bulk vapor at equilibrium with infinite liquid as the droplets get bigger. Table I summarizes these observations, where the radius of a droplet,  $r$ , is calculated by using the relation  $N = \frac{4}{3}\pi r^3 c_l$ , where  $N$  is the total number of moles of water in the system.

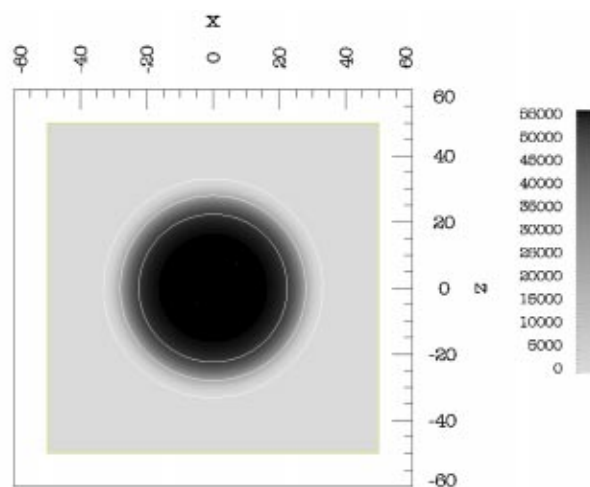


FIG. 13. Cross section through a droplet of  $28 \text{ \AA}$  radius simulated as described in Sec. IV C. Three contour lines for  $55\,000 \text{ mol/m}^3$ ,  $25\,000 \text{ mol/m}^3$ , and  $100 \text{ mol/m}^3$  are shown.

A relation between vapor pressure at equilibrium with a droplet and its radius is given by<sup>41</sup>

$$P_r(T) = P_\infty(T) \exp\left(\frac{2\gamma}{cRT} \frac{1}{r}\right), \quad (48)$$

where  $r$  is the radius of the droplet,  $P_r$  is the temperature-dependent vapor pressure corresponding to a droplet of radius  $r$ ,  $P_\infty$  is the temperature-dependent vapor pressure of a vapor at equilibrium with infinite bulk liquid,  $T$  is the temperature,  $R$  is the gas constant,  $\gamma$  is the coefficient of surface tension, and  $c$  is the density of the liquid inside the droplet. Inherent to this relation is the approximation that the coefficient of surface tension is independent of droplet size.

Taking the logarithm of both sides of this equation, it is seen that

$$\ln(P_r(T)) = \ln(P_\infty(T)) + \frac{2\gamma}{cRT} \frac{1}{r}. \quad (49)$$

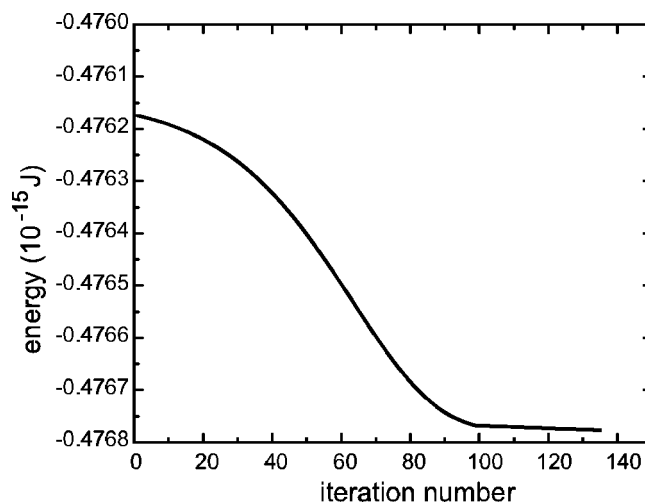


FIG. 14. System free energy as a function of iteration number in simulation of the droplet of radius  $28 \text{ \AA}$  shown in Fig. 13.

TABLE I. Density in the middle of droplets ( $c_m$ ) and of vapor at equilibrium with them ( $c_v$ ), as functions of droplet size.

$r(\text{\AA})$	$c_m(\text{mol/m}^3)$	$c_v(\text{mol/m}^3)$
12.9	58054.4	86.9
20.6	57849.6	45.1
27.8	56901.6	34.2
36.1	56445.6	28.2
46.5	56168.0	25.1
59.2	55937.6	22.7
65.3	55855.6	22.1
91.0	55534.4	19.8

Thus a plot of  $\ln(P_r)$  versus  $1/r$  should yield a straight line whose  $y$ -intercept gives  $P_\infty(300)$  and whose slope gives  $\gamma$ . Such a plot for the data presented in Table I, together with the straight line that fits it best, are shown in Fig. 15. As seen, the fit is very good. The straight line has a  $y$ -intercept of 10.58 and a slope of  $21.7 \text{ \AA}$ . The  $y$ -intercept corresponds to  $P_\infty \approx 39340.1 \text{ Pa}$ , which is 8% lower than the actual vapor pressure exerted by  $c_v$ . Using  $c = c_l$  in the expression for the slope, the fit to the simulation data yields  $\gamma \approx 150 \text{ mN/m}$ , which is 11% higher than the value obtained using Eq. (43).

The results obtained here are acceptable given the many approximations involved in calculating them. First, we are assuming that the coefficient of surface tension does not depend on droplet size, but it has been observed through molecular dynamics simulations that surface tension does depend on it.<sup>8</sup> Second, we have used  $c = c_l$  in Eq. (49), but, as seen from Table I, the density in the middle of the droplet depends on its size as well. Third, the definition of droplet radii is somewhat arbitrary.

Another relation between the radius of a droplet, the pressure inside it ( $P_{\text{in}}$ ), the pressure of the vapor at equilibrium with it ( $P_{\text{out}}$ ) and its surface tension, is the Laplace equation for capillary pressure:<sup>42</sup>

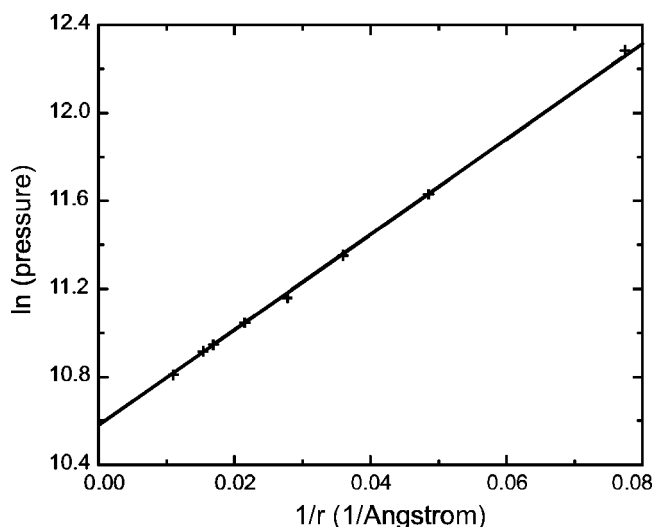


FIG. 15. Natural logarithm of the pressure (in Pa) vs the inverse of droplet radius. The discrete data points are those obtained from the simulations, while the straight line is from the fit to these data points.

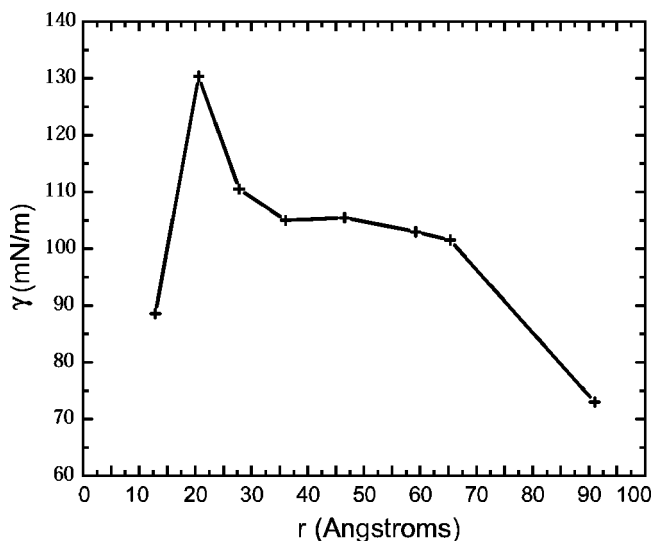


FIG. 16. Surface tension of water droplets in Table I as a function of their radii, calculated using the Laplace equation for capillary pressure [Eq. (50)].

$$\gamma = \frac{r}{2}(P_{\text{in}} - P_{\text{out}}). \quad (50)$$

It is derived by imposing mechanical equilibrium on a “piece” of the droplet’s surface, where the higher pressure inside the droplet is balanced by the pressure of the vapor surrounding the droplet and surface tension. The additional force from surface tension allows the existence of such high densities inside the droplet.

Using the pressure corresponding to the concentration at the center of the droplet as  $P_{\text{in}}$ , the surface tension of the droplets in Table I is plotted in Fig. 16. It is seen that the surface tension increases with radius for small droplets, as observed in previous molecular dynamics simulation results.<sup>8,9</sup> However, the smallest droplet considered here might be too small for Eq. (50) to be valid. For larger droplets, which have more “macroscopic” character, the surface tension decreases with radius. Except for the largest droplet, the surface tension seems to be reaching a plateau at about  $100 \text{ mN/m}$ . Although, apparently coincidentally, the surface tension obtained for the largest droplet lies close to the experimental value of  $72 \text{ mN/m}$ ,<sup>39</sup> it is inconsistent with the rest of our results. The significant decrease in surface tension for the largest droplet might be due to finite system size effects.

Although the accuracy of the values obtained for the surface tension using Eq. (50) is not certain, surface tension values are definitely in qualitative agreement with each other, with the values obtained using Eqs. (43) and (48), and with experimental measurements.<sup>39</sup> More accurate calculations of pressure as a function of space using a mesoscopic formula are under way.<sup>43</sup>

As observed earlier in modeling orientation at the planar interface, the profile of  $\rho^0$  does not change much when the anisotropic term in the free energy is included and the free energy is minimized with respect both to  $\rho^0$  and  $\rho^1$ . Thus the above results are valid in the general case where orientation is accounted for.

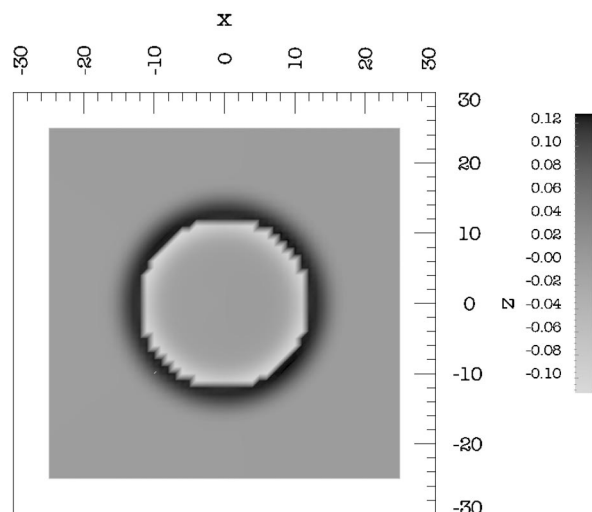


FIG. 17. Cross section through a droplet of radius 20.6 Å. The color scale indicates the value of  $\langle \mathbf{n}_s \cdot \mathbf{n}_s \rangle_{\mathbf{r}}$  as defined in the text.

#### D. Order at the surface of a droplet

As with planar interfaces, the liquid–vapor interface at the surface of a droplet exhibits anisotropy that is not present inside the droplet or in the vapor surrounding it. Figure 17 shows the orientational order at the surface of a droplet whose radius is 20.6 Å. Plotted in the figure is  $\langle \mathbf{n}_s \cdot \mathbf{n}_s \rangle_{\mathbf{r}}$ , where  $\mathbf{n}_s(\mathbf{r})$  is the unit vector normal to the surface at a point  $\mathbf{r}$  and the angle brackets indicate averaging over all angles at that point. As expected, there is no ordering inside the droplet or in the vapor surrounding it. At the interface, the average dipole moment points toward the center on the liquid side of the Gibbs dividing surface [defined in Eq. (38)] and toward the vapor on the vapor side of the Gibbs dividing surface, in agreement with the behavior observed at a planar interface.

Numerically, space was divided into cubic elements of 1 Å sides, while the range of angular coordinates was divided into  $0.1\pi \times 0.1\pi \times 0.1\pi$  elements. The angular discretization was coarse compared to the planar interface case, but this was unavoidable due to computational limitations. Notice, however, that the results obtained in a similar simulation but with half the number of angular elements in each direction (results not shown here) were very close to the results obtained in this simulation. Moreover, since  $\rho^0$  was not expected to change much during the simulation, it was fixed at its initial value to speed up the calculations.

#### V. CONCLUSION

A model that predicts the position-orientation number density of water in mesoscopic structures such as interfaces and droplets has been developed. It is based on an expansion of the Helmholtz free energy about the isotropic state, retaining terms up to first order. The zeroth order term, which has the major contribution, consists of a classical equation of state term and a gradient correction. The first order term, an external potential-like contribution, induces orientational order due to density gradients.

Regarding orientation at the interface, the model reproduces recent molecular dynamics simulation results<sup>7</sup> in detail. It predicts that water molecules orient their dipole moments almost parallel to the interface, pointing with a small angle toward the bulk phase on the side of which they reside. Moreover, there is a tendency to have the molecular plane parallel to the interface on the liquid side and perpendicular to it on the vapor side.

One part of the model that must be improved is the gradient correction in the isotropic part of the free energy. As presented in the examples, the surface tension of the liquid–vapor interface as calculated from our model is almost twice as large as that measured experimentally. Since the first order term in the free energy is much smaller in magnitude than the isotropic part, and since the classical equation of state used in our model generally yields good results,<sup>27</sup> this error in the surface tension is likely a reflection of the shortcomings of the gradient correction used.

Treating water as a continuum using the expression for the free energy developed in this paper is an important step towards the efficient modeling of macromolecules *in vitro* and *in vivo*. Such systems are large and include many water molecules, the explicit treatment of which is time consuming. However, combining the above expression for the Helmholtz free energy of water with an appropriate force field describing interatomic interactions and free energy of solvation will be a much more efficient methodology.<sup>22</sup>

Furthermore, the theoretical framework upon which this water model is based is general and can be used to study other systems as well. It is applicable to liquid crystals, such as to the study of order in a homogeneous ferromagnetic-like material.<sup>22</sup> When generalized to multiple species, this formalism can be applied to the self-assembly of molecules into membranes.<sup>28</sup> Since such systems are very large and difficult to model with atomic detail, a density functional approach like that presented here might make their study more feasible.

#### ACKNOWLEDGMENTS

This research has been funded in part by grants from the Indiana 21st Century Research and Technology Fund (Grant No. 4724753 082003) and the Air Force Research Laboratory/DARPA (Grant No. USAF/F30602-02-2-0001 4324757). K.J. also appreciates funding from the McCormick Science Grant and the Richard Slagle Fellowship.

<sup>1</sup>K. B. Eisenthal, Chem. Rev. (Washington, D.C.) **96**, 1343 (1996).

<sup>2</sup>M. C. Goh, J. M. Hicks, K. Kemnitz, G. R. Pinto, K. Bhattacharyya, K. B. Eisenthal, and T. F. Heinz, J. Phys. Chem. **92**, 5074 (1988).

<sup>3</sup>Q. Du, R. Superfine, E. Freysz, and Y. R. Shen, Phys. Rev. Lett. **70**, 2313 (1993).

<sup>4</sup>M. A. Wilson, A. Pohorille, and L. R. Pratt, J. Phys. Chem. **91**, 4873 (1987).

<sup>5</sup>M. Matsumoto and Y. Kataoka, J. Chem. Phys. **88**, 3233 (1988).

<sup>6</sup>R. S. Taylor, L. X. Dang, and B. C. Garrett, J. Phys. Chem. **100**, 11720 (1996).

<sup>7</sup>V. P. Sokhan and D. J. Tildesley, Mol. Phys. **92**, 625 (1997).

<sup>8</sup>V. V. Zakharov, E. N. Brodskaya, and A. Laaksonen, J. Chem. Phys. **107**, 10675 (1997).

<sup>9</sup>V. V. Zakharov, E. N. Brodskaya, and A. Laaksonen, Mol. Phys. **95**, 203 (1998).

- <sup>10</sup>F. H. Stillinger, Jr. and A. Ben-Naim, *J. Chem. Phys.* **47**, 4431 (1967).
- <sup>11</sup>C. A. Croxton, *Physica A* **106A**, 239 (1981).
- <sup>12</sup>B. Yang, D. E. Sullivan, B. Tjpto-Margo, and C. G. Gray, *J. Phys.: Condens. Matter* **3**, F109 (1991).
- <sup>13</sup>B. Yang, D. E. Sullivan, B. Tjpto-Margo, and C. G. Gray, *Mol. Phys.* **76**, 709 (1992).
- <sup>14</sup>B. Yang, D. E. Sullivan, and C. G. Gray, *J. Phys.: Condens. Matter* **6**, 4823 (1994).
- <sup>15</sup>B. Roux and T. Simonson, *Biophys. Chem.* **78**, 1 (1999).
- <sup>16</sup>H. J. C. Berendsen, J. R. Grigera, and T. P. Straatsma, *J. Phys. Chem.* **91**, 6269 (1987).
- <sup>17</sup>P. Mark and L. Nilsson, *J. Phys. Chem. A* **105**, 9954 (2001).
- <sup>18</sup>W. L. Jorgensen, J. Chandrasekhar, J. D. Madura, R. W. Impey, and M. L. Klein, *J. Chem. Phys.* **79**, 926 (1983).
- <sup>19</sup>M. P. Allen and D. J. Tildesley, *The Computer Simulation of Liquids* (Clarendon, Oxford, 1987).
- <sup>20</sup>H. Goldstein, *Classical Mechanics*, 2nd ed. (Addison-Wesley, Reading, 1980).
- <sup>21</sup>C. G. Gray and K. E. Gubbins, *Theory of Molecular Fluids* (Oxford University Press, Oxford, 1984), Vol. 1.
- <sup>22</sup>K. Jaqaman, Ph.D. thesis, Indiana University, 2003.
- <sup>23</sup>W. H. Press *et al.*, *Numerical Recipes in C*, 2nd ed. (Cambridge University Press, New York, 1992).
- <sup>24</sup>K. Tuncay, L. Jarymowycz, A. Sayyed-Ahmad, and P. Ortoleva, *Mesoscopic Theory of Multiphase Fluids in Complex Media* (unpublished).
- <sup>25</sup>J. N. Reddy, *An Introduction to the Finite Element Method*, 2nd ed. (McGraw-Hill, New York, 1993).
- <sup>26</sup>O. Axelsson, *Iterative Solution Methods* (Cambridge University Press, New York, 1994).
- <sup>27</sup>C. A. Jeffery and P. H. Austin, *J. Chem. Phys.* **110**, 484 (1999).
- <sup>28</sup>P. J. Ortoleva, *Mesoscopic Chemical Physics* (unpublished).
- <sup>29</sup>See, for example, the English translation by J. S. Rowlinson, *J. Stat. Phys.* **20**, 197 (1979).
- <sup>30</sup>S. Fisk and B. Widom, *J. Chem. Phys.* **50**, 3219 (1969).
- <sup>31</sup>J. S. Rowlinson and B. Widom, *Molecular Theory of Capillarity* (Clarendon, Oxford, 1982).
- <sup>32</sup>B. Widom, *Mol. Phys.* **96**, 1019 (1999).
- <sup>33</sup>M. E. Fisher and P. J. Upton, *Phys. Rev. Lett.* **65**, 3405 (1990).
- <sup>34</sup>L. D. Landau and E. M. Lifshitz, *Statistical Physics* (Pergamon, London, 1958).
- <sup>35</sup>A. J. M. Yang, P. D. Fleming III, and J. H. Gibbs, *J. Chem. Phys.* **64**, 3732 (1976).
- <sup>36</sup>R. Evans, *Adv. Phys.* **28**, 143 (1979).
- <sup>37</sup>D. Beaglehole, *J. Phys. Chem.* **91**, 5091 (1987).
- <sup>38</sup>A. Braslau, P. S. Pershan, G. Swislow, B. M. Ocko, and J. Alsnielsen, *Phys. Rev. A* **38**, 2457 (1988).
- <sup>39</sup>R. Cini, G. Loglio, and A. Ficalbi, *J. Colloid Interface Sci.* **41**, 287 (1972).
- <sup>40</sup>M. A. Wilson, A. Pohorille, and L. R. Pratt, *J. Chem. Phys.* **90**, 5211 (1989).
- <sup>41</sup>K. Huang, *Statistical Mechanics*, 2nd ed. (Wiley, New York, 1987).
- <sup>42</sup>J. Bear, *Dynamics of Fluids in Porous Media* (American Elsevier, New York, 1972).
- <sup>43</sup>K. Tuncay, K. Jaqaman, and P. J. Ortoleva, *On the State of Stress and Interfacial Forces in Mesoscopic Systems* (unpublished).